Physics of Plasmas ARTICLE pubs.aip.org/aip/pop

# Effect analysis of spatial discrepancy of secondary emission yield on multipactor formation

Cite as: Phys. Plasmas **30**, 103102 (2023); doi: 10.1063/5.0164977
Submitted: 26 June 2023 · Accepted: 17 September 2023 ·
Published Online: 3 October 2023

View Online

Export Citation

CrossMark

Shu Lin,[1,2] Huan Zhong,[1] Cheng Chen,[1] Meng Cao,[1] Yongdong Li,[1] Yonggui Zhai,[1] Patrick Y. Wong,[1,2,a)] Peng Zhang,[2] and John P. Verboncoeur[2]

## AFFILIATIONS

[1]Key Laboratory for Physical Electronics and Devices of the Ministry of Education, Faculty of Electronic and Information Engineering, Xi'an Jiaotong University, Xi'an, Shaanxi 710049, China
[2]Department of Electrical and Computer Engineering, Michigan State University, East Lansing, Michigan 48824, USA

[a)]Author to whom correspondence should be addressed: huangpatyang@gmail.com

## ABSTRACT

Spatial discrepancy of secondary emission yield (SEY) is probably exacerbated by unexpected surface contamination or imperfect surface treatments for SEY suppression, which accordingly provokes increased multipactor risk in microwave devices. In this paper, an improved 2D2V nonstationary statistical modeling for multipactor of parallel plates capable of regarding all electron impacts and electron exchange at the periodic boundaries is developed to investigate the effect of this spatial SEY discrepancy on multipactor formation in microwave devices. The comparison with the 1D2V statistical modeling results, which is valid for the parallel-plate multipactor, proves the accuracy of this improved 2D2V statistical modeling and the necessity of appropriate boundary setting in multipactor analysis with spatial SEY variation. The modeling results also reveal that the multipactor establishment is dominated by the electron multiplication and the electron overflow in the high-SEY region, thus making the multipactor threshold strongly dependent on both the SEY property and the dimension of the region. Electron multiplication can be fully sustained in the high-SEY region when its size exceeds a critical dimension, which satisfies a scaling law (the sustaining dimension is proportional to the gap with the product of the RF frequency and the gap kept constant) and varies with the involved multipactor mode. This research will help in evaluating accidental multipactor risk caused by the surface contamination and the efficiency of multipactor prevention via applying surface treatments for SEY suppression to accessible regions.

*Published under an exclusive license by AIP Publishing.* https://doi.org/10.1063/5.0164977

03 October 2023 13:18:37

## I. INTRODUCTION

Multipactor[1] is an electron avalanche-like phenomenon ubiquitously occurring in high-power microwave devices and RF components operated under vacuum,[2,3] causing harmful effects such as harmonic noise, cavity detuning, or even irreversible physical damage to the instruments.[4–6] Therefore, it is conventionally required to guarantee no multipactor occurrence in engineering practice for the operational stability of a given microwave system. With the purpose of multipactor prevention in mind, current multipactor research still maintains intense interest in exploring novel multipactor mechanisms[7–10] and developing multipactor inhibition techniques with efficient surface treatments,[11–13] diverse signal waveforms and external fields.[14–16] Meanwhile, accurate predictive techniques[17,18] are highly concerned about the optimal design of multipactor-free microwave devices as well.

As a matter of fact, the values of secondary emission yield (SEY) for multipactor threshold calculations are determined by the average of multiple SEY measurements at different sampled positions on the device surface, but disregard the actual spatial distribution of SEY. Furthermore, this spatial SEY discrepancy or variation always exists because the devices under consideration are fabricated with inevitable differences in the surface composition or roughness, and this is probably exacerbated by local-regional SEY increment due to the induced surface contamination in engineering applications. Industrial convention requires a component to be cleaned to a high standard before the formal system assembly, but despite best efforts, the surface of the component can still become contaminated. According to prior multipactor tests,[19] epoxy glue residue from device fabrication, accidental fingerprints from inappropriate device handling, or contaminated lubricant or dust in a critical area due to incorrect device storage can possibly lead to noticeable threshold decrement. Presently, the underlying multipactor mechanism with partial surface contamination has not been thoroughly analyzed along with the dominant factors affecting multipactor threshold voltage.


Published under an exclusive license by AIP Publishing

This is important not only for the above inevitable reasons but also because of the increasing demand to coat surfaces with specialty coatings[20–22] for multipactor prevention. However, as with the handling of microwave components, this process is not perfect, and the spatial discrepancy of SEY along a surface can also be brought on by incomplete coverage of low-SEY material on the device surface. In particular, it is exceedingly difficult to apply such surface treatments for SEY suppression to the whole device surface, especially within small gaps, which are difficult to access. Furthermore, there may be potential fractional film shedding or rare gas-absorption on the surface during the launch of the satellite-based system as well, thus leading to local-regional SEY increment, despite best efforts for surface cleanliness when on the ground. Another important application where the spatial discrepancy of SEY and its effect on multipactor play a role is in the field of 3D-printed RF components.[23] Using 3D-printing techniques in place of conventional fabrication has garnered intense interest over recent years because of its potential to reduce weight and cost while still maintaining satisfactory performance compared to its metallic counterpart. However, to achieve these comparable effects, the 3D-printed parts have to be coated with a metallic or dielectric layer (using a myriad of methods). This again puts the engineer back to the same fundamental problem as elucidated above relating to imperfect surface treatments leading to local-regional SEY increment.

Multipactor analysis is commonly fulfilled with particle-in-cell[24–26] (PIC) and Monte–Carlo[7,27] simulations, or other novel approaches[28,29] developed recently. Among them, multipactor statistical modeling (STM) is one critical approach that fully regards the stochastic characteristic of secondary electron emission from the probabilistic perspective, thus achieving satisfactory accuracy in multipactor threshold calculations and mechanism analysis.[30] Since first proposed in 2004, statistical modeling has been well developed and widely applied to two-surface multipactor with single-carrier or multi-carrier signal excitation,[30,31] where multipactor analysis is mostly treated as a one-dimensional problem. For better accuracy, 1D2V statistical modeling, which regards transversal electron velocity,[32,33] is then proposed to investigate single-surface multipactor on a dielectric surface. Meanwhile, 2D2V statistical modeling, which also considers the spatial transfer of multipactor electrons, is further developed for multipactor analysis of rectangular waveguides with non-uniform field.[34] However, it disregards the contribution of the single-sided (SS) electron impacts and the electron interactions with the side walls, thus causing inevitable error in the modeling result. Hence, further improvement is still required for the statistical modeling especially when applied to multipactor analysis with the spatial discrepancy of SEY considered.

In this regard, an improved 2D2V nonstationary statistical modeling for multipactor of parallel plates, which regards all types of electron impacts on the surface and electron exchange at the periodic boundary, is developed to analyze the effect of the spatial discrepancy of SEY on multipactor formation. The research content of this paper is organized according to the following sequence. This improved 2D2V statistical modeling is detailed in Sec. II. On that basis, the statistical modeling of the dynamic evolution for parallel-plate multipactor with local-regional SEY variation is performed in Sec. III to explore and understand the underlying mechanism along with PIC simulation. Multipactor threshold analysis involving the critical parameters is executed accordingly in Sec. IV. Finally, the conclusion is provided in Sec. V.

## II. 2D2V NONSTATIONARY STATISTICAL MODELING OF PARALLEL-PLATE MULTIPACTOR

It is noteworthy that the 2D2V nonstationary statistical modeling (simplified as 2D2V statistical modeling below) here is developed for multipactor in parallel plates with uniform field distribution so that the spatial transfer of multipactor electrons only results from the SEY variation at different positions in contrast to the field non-uniformity in multipactor of rectangular waveguides. This improved statistical modeling is essentially extended from previous statistical works in Refs. 34 and 35. In this section, analytical formulation of the 2D2V statistical modeling regarding both contributions of the single-sided (SS) and double-sided (DS) impacts is detailed in Sec. II A along with appropriate setting of electron exchange at the periodic boundary. Afterward, the accuracy of the 2D2V statistical modeling is verified in Sec. II B through the result comparison with the 1D2V statistical modeling.

### A. Basic definitions and formulations

Along the $x$–$y$ coordinates illustrated in Fig. 1, electrons of mass $m$ and charge $e$ are moving between two parallel plates separated by a gap distance of $d$, where the width of the central region and the whole modeling region are $w$ and $l$, respectively. With the sinusoidal electromagnetic field in the dominant TEM mode, the RF electric component for electron acceleration is expressed as $E_{rf}\sin(\omega t)$, where the RF voltage amplitude ($V_{rf}$), the RF frequency ($f$), and the angular frequency ($\omega$) satisfy $V_{rf} = E_{rf}d$ and $\omega = 2\pi f$, respectively. For the convenience of statistical modeling, the following 2D distribution function is assumed for the emission velocities of secondary electrons with anisotropic emission (see Ref. 34 for more detailed derivation):

$$F_{2d}(u_x, u_y) = \frac{\sqrt{2}u_x}{\chi^3\pi^{3/2}}\exp\left(-\frac{u_x^2+u_y^2}{4\chi^2}\right)K_0\left(\frac{u_x^2+u_y^2}{4\chi^2}\right), \quad (1)$$

where $u_x$ and $u_y$ are the vertical ($\upsilon_x$) and transversal ($\upsilon_y$) emission velocities normalized to the oscillation velocity ($\upsilon_\omega$), respectively, with

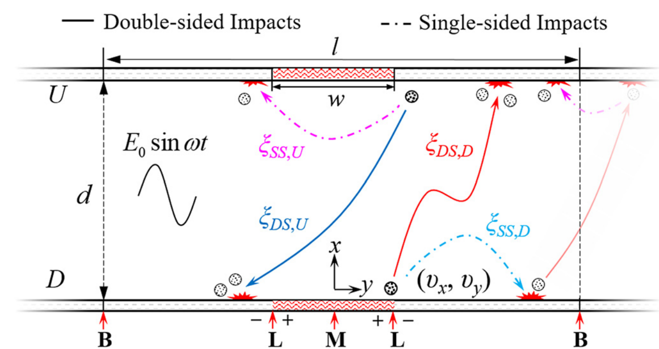


FIG. 1. Illustration of 2D2V statistical modeling for multipactor of parallel plates contributed to by both the double-sided (solid) and single-sided (dashed-dotted) impacts of secondary electrons emitted from different positions on the bottom ($D$) and top ($U$) plates, as well as electron exchange at the periodic boundaries (marked with "B") of the modeling region. The plate separation, the width of the central region, and the whole modeling region are $d$, $w$, and $l$, respectively. The mid-point and the boundary of the central region are marked with "M" and "L" separately, and "+" and "−" refer to the sides of L in the central region and the background region, respectively.

03 October 2023 13:18:37



Published under an exclusive license by AIP Publishing

$\upsilon_\omega = eE_{\rm rf}/m\omega$ and $\chi$ is the ratio of the thermal velocity ($\upsilon_t$) and $\upsilon_\omega$, setting the value of $m\upsilon_t^2/2$ to be 1.5 eV as in previous statistical literature.[31,35]

The analytic solutions for electron motion in both $x$ and $y$ directions can be directly derived from the Lorentz force equation when neglecting the effect of RF magnetic field and further converted into the following expressions:

$$u_x(\tau|\varphi';\xi(\kappa,\varsigma)) = \frac{\kappa - \sin\varphi' + \sin(\varphi'+\tau) - \tau\cos\varphi'}{\varsigma\tau}, \tag{2}$$

$$u_y(\eta|\tau,\eta') = \frac{\eta-\eta'}{\tau}, \tag{3}$$

where $\varphi'$ and $\tau$ are the electron emission phase and transit time (the phase variation at electron impacts), respectively; $\eta'$ and $\eta$ are the normalized emission and impact positions along the $y$ direction separately; $\kappa$ signifies the normalized position displacement along the $x$ direction; and $\varsigma$ is the sign of electron motion direction, which is positive and negative separately for electron emissions from the bottom and top plates (differentiated with the subscripts of "$D$" and "$U$"). Thus, electron trajectories ($\xi$) can be categorized into four different cases according to electron impact type (first subscript) and emission position (second subscript), having $\xi_{{\rm SS},D}$ $(\kappa=0|\,\varsigma=1)$, $\xi_{{\rm DS},D}$ $(\kappa=\lambda|\,\varsigma=1)$, $\xi_{{\rm SS},U}$ $(\kappa=0|\,\varsigma=-1)$, and $\xi_{{\rm DS},U}$ $(\kappa=-\lambda|\,\varsigma=-1)$, where $\lambda=\omega d/\upsilon_\omega$.

On that basis, the joint probability density function (JPDF) denoted as $G(\tau,\eta|\varphi',\eta';\xi)$, which physically accounts for the probability density of electrons emitted at phase $\varphi'$ and position $\eta'$ and then impact at position $\eta$ with transit time $\tau$ after experiencing the specified trajectory $\xi$, can be constructed with the following expression:

$$G(\tau,\eta|\varphi',\eta';\xi) = F_{2d}\left[g_x(\tau|\varphi';\xi), u_y(\eta|\tau,\eta')\right] \times\left|\frac{dg_x(\tau|\varphi';\xi)}{d\tau}\right|\times\left|\frac{du_y(\eta|\tau,\eta')}{d\eta}\right|, \tag{4}$$

where $g_x(\tau|\varphi';\xi)$ is a monotonic function obtained from the function $u_x(\tau|\varphi';\xi)$ by removing all its non-monotonic intervals; see Refs. 31 and 34 for more details.

With the above-constructed JPDF, the 2D2V statistical modeling for multipactor dynamic analysis then can be fulfilled through the deduction of the rate parameters for electron emission and impact (unit: rad$^{-1}$·mm$^{-1}$) on the bottom and top surfaces. Taking the bottom surface, for example, electron emission and impact rates [$C_D(\varphi,\eta)$ and $I_D(\varphi,\eta)$] are contributed to by both the DS impacts of electrons emitted from the top surface and the SS impacts of electrons emitted from the bottom surface. It is impractical to cover multipactor evolution within infinite plates, so the statistical formulations below involve electron emissions at different positions of either surface within the time window $[0,\varphi]$ and the limited position range $[-\eta_b,\eta_b]$, yielding

$$\begin{aligned}C_D(\varphi,\eta) &= \int_{-\eta_b}^{\eta_b} d\eta'\int_0^{\varphi} C_D(\varphi',\eta')K_{{\rm SS},D}(\varphi-\varphi',\eta|\varphi',\eta';\xi_{{\rm SS},D})d\varphi' \\ &+\int_{-\eta_b}^{\eta_b} d\eta'\int_0^{\varphi} C_U(\varphi',\eta')K_{{\rm DS},U}(\varphi-\varphi',\eta|\varphi',\eta';\xi_{{\rm DS},U})d\varphi' \\ &+S_D(\varphi,\eta)+S_U(\varphi,\eta)+\psi_D(\varphi,\eta)\end{aligned} \tag{5}$$

and

$$\begin{aligned}I_D(\varphi,\eta) &= \int_{-\eta_b}^{\eta_b} d\eta'\int_0^{\varphi} C_D(\varphi',\eta')G_{{\rm SS},D}(\varphi-\varphi',\eta|\varphi',\eta';\xi_{{\rm SS},D})d\varphi' \\ &+\int_{-\eta_b}^{\eta_b} d\eta'\int_0^{\varphi} C_U(\varphi',\eta')G_{{\rm DS},U}(\varphi-\varphi',\eta|\varphi',\eta';\xi_{{\rm DS},U})d\varphi' \\ &+B_D(\varphi,\eta)+B_U(\varphi,\eta),\end{aligned} \tag{6}$$

where $\eta_b$ is the normalized boundary of the modeling region, having $\eta_b=\omega l/2\upsilon_\omega$ and $\tau=\varphi-\varphi'$; $\Psi(\varphi,\eta)$ refers to the external seeding source. It is worth noting that multipactor formation is actually contributed to by all electron emissions from different positions, while the integrations in Eqs. (5) and (6) only regard the counterpart of electron emissions inside the modeling region. Hence, the contributions from electron emissions outside the boundary are compensated by adding the terms of $S(\varphi,\eta)$ and $B(\varphi,\eta)$ in the above formulations, and the related expressions for the bottom portion are as follows:

$$\begin{aligned}S_D(\varphi,\eta) &= \int_{-\infty}^{-\eta_b} d\eta'\int_0^{\varphi} C_D(\varphi',-\eta_b)K_{{\rm SS},D}(\varphi-\varphi',\eta|\varphi',\eta';\xi_{{\rm SS},D})d\varphi' \\ &+\int_{-\infty}^{-\eta_b} d\eta'\int_0^{\varphi} C_U(\varphi',-\eta_b)K_{{\rm DS},U}(\varphi-\varphi',\eta|\varphi',\eta';\xi_{{\rm DS},U})d\varphi' \\ &+\int_{\eta_b}^{\infty} d\eta'\int_0^{\varphi} C_D(\varphi',\eta_b)K_{{\rm SS},D}(\varphi-\varphi',\eta|\varphi',\eta';\xi_{{\rm SS},D})d\varphi' \\ &+\int_{\eta_b}^{\infty} d\eta'\int_0^{\varphi} C_U(\varphi',\eta_b)K_{{\rm DS},U}(\varphi-\varphi',\eta|\varphi',\eta';\xi_{{\rm DS},U})d\varphi'\end{aligned} \tag{7}$$

and

$$\begin{aligned}B_D(\varphi,\eta) &= \int_{-\infty}^{-\eta_b} d\eta'\int_0^{\varphi} C_D(\varphi',-\eta_b)G_{{\rm SS},D}(\varphi-\varphi',\eta|\varphi',\eta';\xi_{{\rm SS},D})d\varphi' \\ &+\int_{-\infty}^{-\eta_b} d\eta'\int_0^{\varphi} C_U(\varphi',-\eta_b)G_{{\rm DS},U}(\varphi-\varphi',\eta|\varphi',\eta';\xi_{{\rm DS},U})d\varphi' \\ &+\int_{\eta_b}^{\infty} d\eta'\int_0^{\varphi} C_D(\varphi',\eta_b)G_{{\rm SS},D}(\varphi-\varphi',\eta|\varphi',\eta';\xi_{{\rm SS},D})d\varphi' \\ &+\int_{\eta_b}^{\infty} d\eta'\int_0^{\varphi} C_U(\varphi',\eta_b)G_{{\rm DS},U}(\varphi-\varphi',\eta|\varphi',\eta';\xi_{{\rm DS},U})d\varphi'.\end{aligned} \tag{8}$$

As can be seen, the above integrations for the boundary compensation (abbreviated as BC below) only involve electron emission rates right at the boundaries, which are adopted to approximate electron emission rates outside the modeling region. This is valid for $l \gg w$ since electron emissions at the boundary and outside the modeling region are hardly affected by the SEY variations in the central region and, thus, are determined with the same field condition and background SEY property. To the best of the authors' knowledge, this is the first time adopting the above complementary terms for the 2D2V statistical formulations of parallel-plate multipactor with periodic boundary setting.

Note that the relevant parameters of the top surface can be formulated analogously by converting the subscripts of the involved parameters in Eqs. (5)–(8). Accordingly, the spatial population density [$E(\varphi,\eta)$] and the total population number [$N(\varphi)$] of multipactor electrons generated inside the gap at phase $\varphi$ are separately expressed as

03 October 2023 13:18:37



Published under an exclusive license by AIP Publishing

$$E(\varphi,\eta)=\int_0^{\varphi}C(\varphi',\eta)-I(\varphi',\eta)d\varphi', \tag{9}$$

$$N(\varphi)=\int_{-\eta_b}^{\eta_b}E(\varphi,\eta')d\eta', \tag{10}$$

where $C(\varphi,\eta)=C_D(\varphi,\eta)+C_U(\varphi,\eta)$ and $I(\varphi,\eta)=I_D(\varphi,\eta)+I_U(\varphi,\eta)$, and the component function $K(\tau,\eta|\varphi',\eta';\xi)$ in Eqs. (5) and (7) is written as

$$K\left(\tau,\eta|\varphi',\eta';\xi\right)=G\left(\tau,\eta|\varphi',\eta';\xi\right)\sigma\left(\tau,\eta|\varphi',\eta';\xi\right), \tag{11}$$

where $G(\tau,\eta|\varphi',\eta';\xi)$ is the JPDF predefined in Eq. (4) and $\sigma(\tau,\eta|\varphi',\eta';\xi)$ is the function adopted for calculating the related production of secondary electrons. It is actually fulfilled by substituting the corresponding impact energy ($W_p$) and impact angle ($\theta_p$) of electron trajectory $\xi$ into the position-dependent empirical formula of SEY [$\delta(W_p,\theta_p,\eta)$] and expressed below for the case with the central SEY variation as illustrated in Fig. 1,

$$\delta\left(W_p,\theta_p,\eta\right)=\begin{cases}\delta_c(W_p,\theta_p), & \eta_c>|\eta|\ge 0,\\ \delta_b(W_p,\theta_p), & \eta_b>|\eta|\ge\eta_c,\end{cases} \tag{12}$$

where $\delta_c(W_p,\theta_p)$ and $\delta_b(W_p,\theta_p)$, respectively, refer to Furman's SEY formula of the central and background material; $\eta_c$ is the normalized boundary of the central region, having $\eta_c=\omega w/2v_\omega$.

The 2D2V statistical formulations above eventually constitute the system of Volterra integral equations, which are, thus, solved to model multipactor dynamic evolution regarding the spatial distribution of SEY. Accordingly, the effective SEY ($\sigma_{\rm eff}$) for determining the variation trend of electron population can be calculated with

$$\sigma_{\rm eff}=\frac{\int_{-\eta_b}^{\eta_b}d\eta'\int_{\varphi_t}^{\varphi}(C_D(\varphi',\eta')+C_U(\varphi',\eta'))d\varphi'}{\int_{-\eta_b}^{\eta_b}d\eta'\int_{\varphi_t}^{\varphi}(I_D(\varphi',\eta')+I_U(\varphi',\eta'))d\varphi'}, \tag{13}$$

where the time window $[\varphi_t,\varphi]$ is usually set in the steady-state stage of multipactor evolution and multipactor apparently occurs when $\sigma_{\rm eff}$ is larger than unity. The onset condition of multipactor is determined with $\sigma_{\rm eff}=1$ for the threshold calculation.

## B. Result verification

Strictly speaking, the above 2D2V statistical modeling still requires further verification before its practical application to multipactor analysis. Therefore, the result comparison of 2D2V and 1D2V statistical modeling is first conducted for multipactor between parallel plates with a uniform coating of silver (Ag);[19] see main SEY parameters in Table I. It is worth noting that the 1D2V statistical modeling for this comparison is fulfilled by converting the above 2D JPDF into the 1D JPDF through the integral of $\eta$, then adopting the 1D nonstationary statistical description as in previous statistical literature.[31,35] It actually regards angular emission and impact of electrons but disregards the spatial transfer of electrons between different positions for its spatial uniformity during multipactor formation of parallel plates with uniform SEY distribution.

The detailed evolutions of the total population number and the spatial population density of multipactor electrons for three different cases with the RF voltage above ($V_{\rm rf}=110$ V), at the threshold ($V_{\rm rf}=100.4$ V) and below ($V_{\rm rf}=90$ V) the breakdown level, are calculated and plotted in Figs. 2 and 3, respectively, where $fd=1.64$ GHz·mm. The external seeding in the 2D2V statistical modeling is set spatially uniform at $\varphi=0$, and the 1D2V modeling results with the same seeding amount are also provided to compare the results of the 2D2V statistical modeling with and without BC, which actually refer to the complementary contributions of electron emissions outside of the modeling region corresponding to the terms of $S(\varphi,\eta)$ and $B(\varphi,\eta)$ in Eqs. (7) and (8). Note that the sinusoidal behavior of the RF field inherently leads to the oscillations in the results [see the inset window in the threshold-breakdown result of Fig. 3(a)], so here the periodic average of the involved parameters (denoted with a bar) is actually adopted for better illustration of the variation trend.

As can be seen in Fig. 3(a), the distributions of the spatial population density are kept uniform during the whole multipactor dynamic evolution for all of the 2D2V results with BC. Meanwhile, the time evolutions of the total electron population in the 1D2V results perfectly overlap with those of the 2D2V results in all the above cases, thus proving the result accuracy of 2D2V statistical modeling with BC.

**TABLE I.** Main SEY constants of the involved materials.

| Material | $\sigma_m$ | $E_m$/eV | $E_1$/eV | $E_2$/eV |
|---|---|---|---|---|
| Ag | 2.25 | 165 | 20.5 | 5000 |
| Cu | 2.48 | 304.8 | 18.6 | 4000 |
| Au | 1.8 | 1000 | 174.3 | 4000 |
| Micro-structured Au[a] | 1.12 | 1200 | 500 | 3650 |

[a]Lower-SEY Au obtained with surface treatment in Ref. 21.

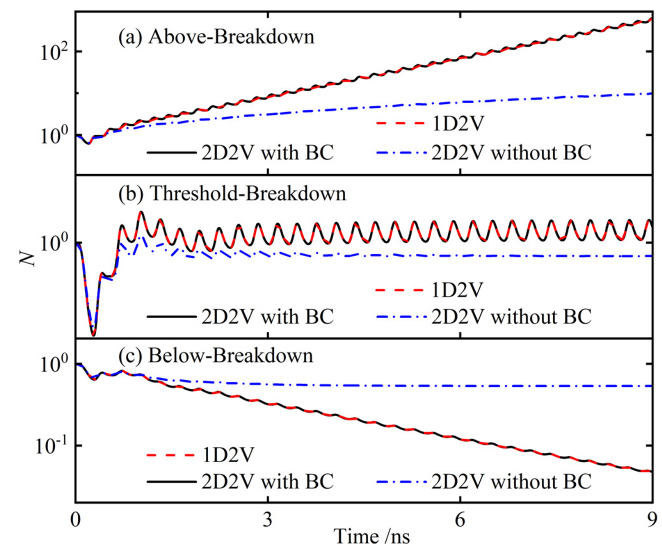


**FIG. 2.** Time evolution of the total population number of multipactor electrons in parallel plates with uniform surface coating of Ag for different cases with the RF voltages above (a), at the threshold (b) and below (c) the breakdown level, where $fd=1.64$ GHz·mm and $l=1.0$ mm. The 1D2V statistical modeling results (red dashed) are compared with the results of the 2D2V statistical modeling with (black solid) and without (blue dotted-dashed) the boundary compensation (BC).

03 October 2023 13:18:37


Published under an exclusive license by AIP Publishing

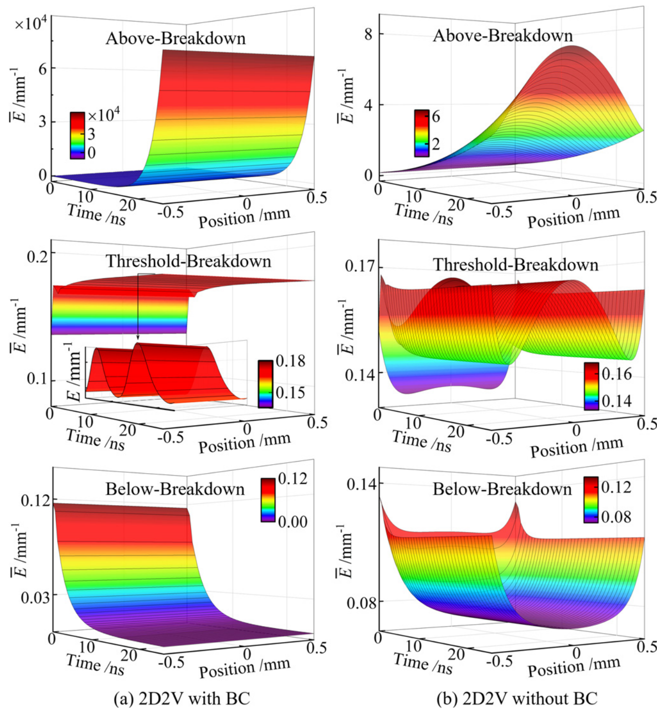


**FIG. 3.** Time evolution of periodic average of the spatial population density [$\bar{E}(t, y)$] obtained from the 2D2V statistical modeling with (a) and without (b) the boundary compensation (BC) for different multipactor cases with the RF voltages above, at the threshold and below multipactor breakdown level. The other parameters are as in Fig. 2.

Meanwhile, the neglect of BC causes apparent variation of the total population number in the 2D2V results and also makes the spatial population density turn non-uniform as shown in Fig. 3(b). In the above-breakdown case, electron impacts are more likely to generate net electron emissions with high impact energy, and the 2D2V statistical modeling without BC disregards the contribution of electron emissions outside the modeling region, thus causing more electron loss at the position closer to both boundaries. Hence, it eventually forms less of an increment in the total population number and more of a parabolic-like distribution in the spatial population density. This correspondingly results in less of a decrement in electron population and inverse density distribution as a result of net electron absorption with lower impact energy in the below-breakdown case. While for the threshold-breakdown case, the electron loss also leads to a slight decrement in the total population number and a "w-type" spatial distribution in the overall population density, which is also different from the uniform distribution in the 2D2V results with BC. Hereby, the above result comparison essentially reveals the significance of appropriate boundary setting in the 2D2V statistical modeling, which is, thus, adopted by default in the following multipactor analysis when regarding the spatial distribution of SEY.

## III. MULTIPACTOR DYNAMIC MODELING WITH SPATIAL SEY DISCREPANCY

For a preliminary analysis, the multipactor dynamic evolution in parallel plates with a patchy SEY distribution is modeled with CST (computer simulation technology) Particle Studio. Referencing circular electron beams utilized in practical SEY measurements, the spatial SEY distribution is approximately characterized/modeled with local SEY variations in several circular regions on both plates, where the surface state is disregarded and the secondary emission property in the different regions is only determined with the material type. Each region of specified diameter is uniformly coated with one single material different from the plate (background) material as illustrated in Fig. 4. Meanwhile, they are also distributed far away from each other so that the regional electron multiplication is only affected by their own dimensions and SEY properties. Using gold[19] (Au) as the background material of the plate surface, the diameters and the materials in each circular region are, respectively, set with $R_1(w = 2.0\,\text{mm}$, silver), $R_2(w = 1.0\,\text{mm}$, silver), and $R_3[w = 1.0\,\text{mm}$, copper[36] (Cu)], and the first crossover energy of the involved materials are ordered as Cu < Ag < Au according to the main SEY constants listed in Table I. Note that this paper adopts the previous ECSS (European Cooperation for Space Standardization) standard, which has been extensively used in past multipactor research so that the modeling results here can be more easily compared with the previous ones. Moreover, adopting materials with much different SEY also helps to better illustrate the effect of the SEY property on multipactor formation. Meanwhile, Furman's SEY formula[37] is adopted in both the PIC simulation and the 2D2V statistical modeling for the following multipactor analysis, and the applied RF voltage ($V_{rf}$) is set with $V_{tl} < V_{rf} < V_{th}$ where $V_{tl}(V_{th})$ refers to the multipactor threshold voltages of parallel plates with both plate surfaces fully coated by Ag(Au). It can be seen that the electron multiplication is generated in $R_1$ because of its relatively higher SEY, but the region shrinkage in $R_2$ and $R_3$ and further SEY increment in $R_3$ eventually result in an opposite trend for the electron population in these two regions. This reveals a higher potential risk of multipactor provoked by the surface contamination with high SEY and the significant effects of

03 October 2023 13:18:37

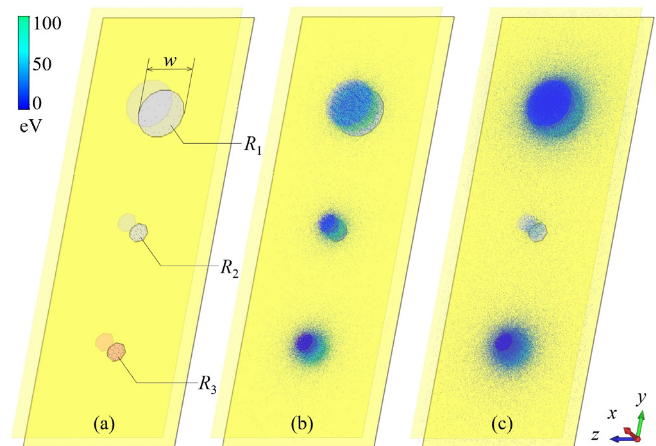


**FIG. 4.** Spatial distributions of multipactor electrons at the beginning (a) and the end (b) of the seeding stage and simulation termination (c) during multipactor formation in parallel plates with a patchy SEY distribution. The diameters and the material in each region are set with $R_1(w = 2.0\,\text{mm}$, Ag), $R_2(w = 1.0\,\text{mm}$, Ag), and $R_3(w = 1.0\,\text{mm}$, Cu), respectively, and the background material of the plate surface is Au. The applied RF voltage ($V_{rf}$) is set between the multipactor threshold voltages with both plate surfaces fully coated with Ag and Au for $fd = 1.64$ GHz·mm.


Published under an exclusive license by AIP Publishing

the width and the SEY property of the local high-SEY region on multipactor formation.

For comparison, the above 2D2V statistical modeling (STM) is also adopted here for the mechanism analysis of multipactor formation with local-regional SEY increment, albeit simplified as a 2D problem according to the distribution symmetry of multipactor electrons as revealed above. The time evolutions of the periodically averaged emission rate [$\bar{C}(t, y)$], impact rate [$\bar{I}(t, y)$], and population density [$\bar{E}(t, y)$] of multipactor electrons for similar parameters as in Fig. 4 are provided in Fig. 5. Meanwhile, the oscillating details of these parameters sampled at the mid-point and the boundary of the central region ("M" and "L" marked in Fig. 1 and denoted in subscripts for differentiation) are also provided in Fig. 6 with the total electron population [$N(t)$]. We can see that the trends of electron population obtained from STM are consistent with the above PIC results for all cases of $R_{1-3}$. We can also see in Fig. 5 that the spatial SEY discrepancy causes electron multiplication and absorption in the central region and its surroundings separately and forms a step-like distribution in an electron emission rate with initially

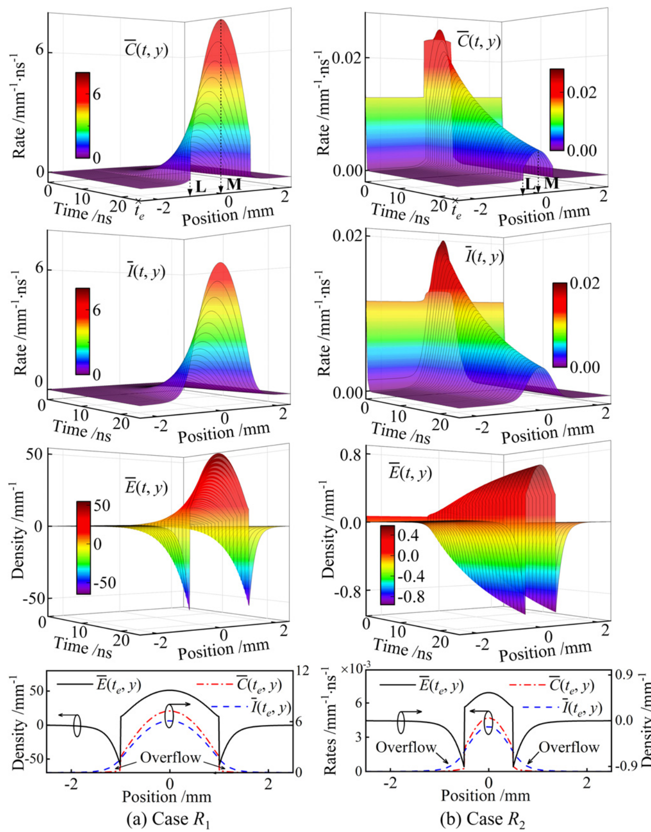


FIG. 5. Time evolution of the periodic average of electron emission rate [$\bar{C}(t, y)$], impact rate [$\bar{I}(t, y)$], and the spatial population density [$\bar{E}(t, y)$] obtained from 2D2V statistical modeling of Case $R_1$(a) and $R_2$(b) in Fig. 4. The sampled distributions of these involved parameters at the modeling termination ($t_e$) are provided in the last row, and the spatial maxima of rate parameters and the sudden drop of population density are located at the mid-point and the boundary of the central region marked with "M" and "L" in Fig. 1 separately. The other parameters are as in Fig. 4.

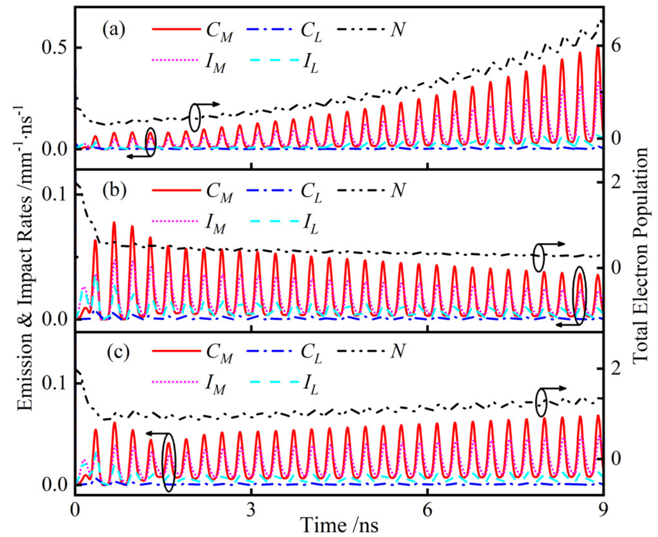


FIG. 6. Time evolution of electron emission and impact rates at the sampled locations of "M" and "L" and the total electron population for the cases of $R_1$(a), $R_2$(b), and $R_3$(c) involved in Fig. 4. The other parameters are as in Fig. 4.

uniform seeding. This can well explain that practical surface damage accumulated during multipactor experimental tests is observed at specific spots rather than the whole region. In the meantime, angular emission of secondary electrons also leads to spatial transfer of multipactor electrons between adjacent regions, and the resultant electron overflow accordingly results in a gradual decrement of electron impact rate outward from the central region. Specifically for the boundary point of L, there are almost same amount of electrons impacting at $L^-$ and $L^+$, which separately refer to one boundary side in the background region and another side in the central region as illustrated in Fig. 1. However, in contrast to electron multiplication at the high-SEY point $L^+$, relatively low SEY at $L^-$ eventually leads to a sudden drop of the electron emission rate and a negative population density, which physically accounts for electron absorption at $L^-$.

As with the case of $R_1$, the population increment for electron multiplication in the high-SEY region exceeds the population loss due to the electron overflow, so there still manifests nearly exponential growth of the total electron population in the whole region as shown in Fig. 6(a). However, the electron overflow is exacerbated with the shrinkage of the high-SEY region and, thus, makes the total electron population decrease as revealed in Fig. 6(b). In the meantime, Fig. 6(c) also shows that the electron multiplication in the central region enhanced with higher-SEY material converts the population trend back to exponential growth. This further evinces the significant effects of the width and the material (SEY property) of the high-SEY region on multipactor formation as revealed above. On the other hand, the final distribution of the spatial population density plotted in the last row of Fig. 5 also reveals that the spatial transfer of electron population ultimately results in the highest density of net electron production near the boundary of the high-SEY region, which can cause charge accumulation on the dielectric surface in dielectric multipactor.[8] It is also worth mentioning that the resultant non-uniform electrostatic field

03 October 2023 13:18:37


Published under an exclusive license by AIP Publishing

from local-regional SEY increment probably exerts a strong effect on multipactor dynamic evolution.

## IV. MULTIPACTOR THRESHOLD ANALYSIS WITH SPATIAL SEY DISCREPANCY

To further investigate the above effects on the multipactor onset condition, the corresponding calculation results of the multipactor threshold voltages ($V_{tt}$) are plotted in Fig. 7. We can see in Fig. 7(a) that $V_{tt}$ is inversely correlated with $w$ and gradually converges to $V_{tl}$ with the increase in $w$ in both the CST and STM results, which are in good agreement. It can also be seen that the induced high-SEY region with millimeter scale can significantly decrease the multipactor threshold and, thus, result in more multipactor risk in practical device operations. In the meantime, the electron multiplication in the high-SEY region can fully predominate multipactor formation in the whole region with $w$ approaching the centimeter scale. The critical dimension ($w_s$) for self-sustaining multipactor in the high-SEY region can be determined by curve-fitting the $V_{tt}$-$w$ data ($w > 1$) with an exponential-decay function in the form of $Ae^{-4.6w/w_s}$, see the specific parameter values for the different conditions of Fig. 7 in Table II. We can also see a significant increase in $w_s$ with mode conversion from first-order (P$_1$, $fd = 1.64$ GHz·mm) to high-order multipactor (P$_2$, $fd = 5.0$ GHz·mm), where the longer transit time inherently results in larger transversal transfer of multipactor electrons.

It is also shown in Fig. 7(b) that further SEY increase in the high-SEY region brought on by replacing Ag with Cu, eventually results in a notable decrease in $V_{tt}$ but little variation in $w_s$. This indicates that it is more prone to provoke accidental multipactor occurrence during practical device operation when inducing surface contamination with higher SEY. Conversely, the decrease in the SEY of the background material can cause an observable increase in the threshold as well, but only when the high-SEY region has a sub-millimeter width (<10% threshold decrease when adopting the micro-structured Au[21] listed in Table I as the background material). This is because the background SEY variation indirectly affects the electron multiplication in the high-SEY region through the interactive exchange of multipactor electrons between the adjacent regions. Meanwhile, the unchanged results of $V_{tt}$ with $d$ doubled but $fd$ kept constant shown in Fig. 7(b) also proves the validity of the scaling law, where $w_s$ is proportional to $d$ with $fd$ kept constant. It is worthy mention that similar mechanism and scaling law can also be found in multipactor of waveguide irises where the electron overflow between different regions is caused by the spatial discrepancy of the RF field; see Ref. 38 for more details. Hence, it is still feasible to prevent multipactor by merely applying the surface treatments of SEY suppression to the accessible regions with small difficult-to-access gaps excluded, and its efficiency can be optimized with higher multipactor mode or lower operation frequencies.

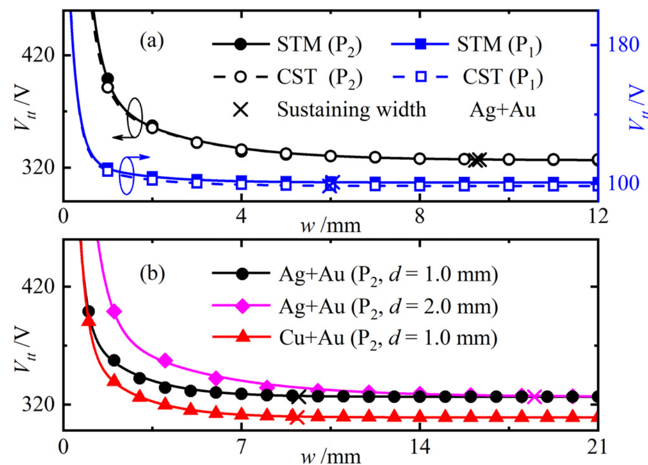


**FIG. 7.** Multipactor threshold voltage ($V_{tt}$) vs the width of high-SEY region ($w$) obtained with STM (solid) and CST (hollow) simulation. Multipactor threshold results of P$_2$ (black circle, $fd = 5.0$ GHz·mm) and P$_1$ (blue rectangle, $fd = 1.64$ GHz·mm) with different multipactor order are compared in (a), and the threshold results of P$_2$ with $d$ doubled (magenta diamond) and with further SEY increase in high-SEY region by replacing Ag with Cu (red triangle) are provided in (b).

**TABLE II.** Parameter values for different conditions in Fig. 7.

| Condition | $w_s(A)$ STM | $w_s(A)$ CST |
|---|---|---|
| Ag + Au (P$_1$, $d = 1.0$ mm) | 6.046 (15.44) | 5.973 (16.27) |
| Ag + Au (P$_2$, $d = 1.0$ mm) | 9.248 (77.28) | 9.34 (75.51) |
| Ag + Au (P$_2$, $d = 2.0$ mm) | 18.49 (77.28) | ··· |
| Cu + Au (P$_2$, $d = 1.0$ mm) | 9.183 (78.81) | ··· |

## V. CONCLUSION

In this paper, an improved 2D2V nonstationary statistical model of parallel-plate multipactor, which is capable of regarding both the single-sided and double-sided impacts as well as electron exchange at the periodic boundaries, is developed to investigate the effect of the spatial discrepancy of the secondary emission yield (SEY) on multipactor formation along with PIC simulation. Exact agreement is found between the results of 1D2V and 2D2V statistical modeling for multipactor between parallel plates with a uniform SEY distribution, which reveals the accuracy of the 2D2V statistical modeling and the necessity of appropriate boundary setting. The threshold analysis reveals that the multipactor onset condition is greatly affected by the electron multiplication in the high-SEY regions. It can fully dominate multipactor development in the whole region when the width of the high-SEY region is increased up to the centimeter scale. We also found that the dimension for multipactor self-sustaining in the high-SEY region increases with higher multipactor order, where the longer transit time of multipactor electrons inherently results in larger transversal transfer. In addition, the sustaining dimension satisfies a scaling law for its proportional relation to the gap with constant product of the RF frequency and the gap. These features are similar to those of multipactor in waveguide irises where the electron spatial overflow between different regions is caused by the spatial discrepancy of the RF field. This research not only evinces the significant effect of local-regional SEY increment from surface contamination on multipactor threshold but also provides a valuable reference to evaluate the efficiency of multipactor prevention by merely applying the surface treatments of SEY suppression to microwave devices, which include small difficult-to-access gaps.

## ACKNOWLEDGMENTS

This research was supported by the National Natural Science Foundation of China (Grant Nos. 61801370, 61971342, and

03 October 2023 13:18:37



Published under an exclusive license by AIP Publishing

U1537210), the Air Force of Scientific Research (AFOSR) MURI (Grant Nos. FA9550-18-1-0062 and FA9550-21-1-0367), and HPC Platform, Xi'an Jiaotong University.

## AUTHOR DECLARATIONS

### Conflict of Interest

The authors have no conflicts to disclose.

### Author Contributions

**Shu Lin:** Investigation (equal); Writing – original draft (equal); Writing – review & editing (equal). **Huan Zhong:** Software (lead); Validation (equal). **Cheng Chen:** Software (equal). **Meng Cao:** Funding acquisition (equal). **Yongdong Li:** Funding acquisition (equal). **Yonggui Zhai:** Software (equal). **Patrick Pat-Yeung Wong:** Software (equal); Validation (equal); Writing – original draft (equal); Writing – review & editing (equal). **Peng Zhang:** Funding acquisition (equal); Writing – review & editing (equal). **John P. Verboncoeur:** Funding acquisition (equal).

## DATA AVAILABILITY

The data that support the findings of this study are available from the corresponding author upon reasonable request.

## REFERENCES


[1] J. R. M. Vaughan, IEEE Trans. Electron Devices **35**(7), 1172 (1988).
[2] D. Gonzalez-Iglesias, D. Esperante, B. Gimeno, C. Blanch, N. Fuster-Martinez, P. Martinez-Reviriego, P. Martin-Luna, J. Fuster, and D. Alesini, IEEE Trans. Electron Devices **70**(1), 288 (2023).
[3] J. Vague, J. C. Melgarejo, M. Guglielmi, V. E. Boria, S. Anza, C. Vicente, M. R. Moreno, M. Taroncher, B. Gimeno Martinez, and D. Raboso, IEEE Trans. Microwave Theory Tech. **66**(8), 3644 (2018).
[4] R. Udiljak, D. Anderson, P. Ingvarson, U. Jordan, U. Jostell, L. Lapierre, G. Li, M. Lisak, J. Puech, and J. Sombrin, IEEE Trans. Plasma Sci. **31**(3), 396 (2003).
[5] D.-Q. Wen, P. Zhang, J. Krek, Y. Fu, and J. P. Verboncoeur, Phys. Rev. Lett. **129**(4), 045001 (2022).
[6] P. Y. Wong, Y. Y. Lau, P. Zhang, N. Jordan, R. M. Gilgenbach, and J. Verboncoeur, Phys. Plasmas **26**(11), 112114 (2019).
[7] X. Zhang, Q. Yu, and X. Ni, IEEE Trans. Electron Devices **69**(2), 748 (2022).
[8] Y. Zhai, H. Wang, M. Cao, M. Weng, S. Lin, M. Peng, K. Chen, R. Wang, Y. Li, W. Cui, J. Chen, and Y. Li, J. Appl. Phys. **131**(9), 093303 (2022).
[9] G.-Y. Sun, B.-P. Song, B.-H. Guo, R.-D. Zhou, S. Zhang, H.-B. Mu, and G.-J. Zhang, J. Phys. D: Appl. Phys. **51**(29), 295201 (2018).
[10] Z. Zhang, Y. Sun, W. Cui, H. Zhang, Y. Huang, and C. Chang, IEEE Trans. Electron Devices **66**(11), 4921–4927 (2019).
[11] M. Mirmozafari, A. Iqbal, P. Zhang, N. Behdad, J. H. Booske, and J. P. Verboncoeur, Phys. Plasmas **29**(8), 082109 (2022).
[12] C. Chang, Y. D. Li, J. Verboncoeur, Y. S. Liu, and C. L. Liu, Phys. Plasmas **24**(4), 040702 (2017).
[13] C. H. Chen, C. Chang, W. Y. Liu, J. Sun, H. J. Huang, C. F. Ke, W. Song, Y. Teng, X. L. Wu, J. L. Xie, M. Zhu, S. Li, J. P. Fang, P. Wu, and L. J. Zhang, J. Appl. Phys. **114**(16), 163304 (2013).
[14] D.-Q. Wen, A. Iqbal, P. Zhang, and J. P. Verboncoeur, Phys. Plasmas **26**(9), 093503 (2019).
[15] C. Chang, G. Z. Liu, C. X. Tang, C. H. Chen, H. Shao, and W. H. Huang, Appl. Phys. Lett. **96**(11), 111502 (2010).
[16] C. Jing, C. Chang, S. H. Gold, R. Konecny, S. Antipov, P. Schoessow, A. Kanareykin, and W. Gai, Appl. Phys. Lett. **103**(21), 213503 (2013).
[17] L. Silvestre, Z. C. Shaw, T. Sugai, J. Stephens, J. J. Mankowski, J. Dickens, A. A. Neuber, and R. P. Joshi, J. Phys. D **55**(4), 045202 (2022).
[18] M. Siddiqi and R. A. Kishek, Phys. Plasmas **26**(4), 043104 (2019).
[19] ECSS Secretariat, "ESA-ESTEC requirements and standards division," ESA-ESTEC Report No. ECSS-E-20-01A Rev. 1 (2013).
[20] G. Troncoso, J. M. Garcia-Martin, M. U. Gonzalez, C. Morales, M. Fernandez-Castro, J. Soler-Morala, L. Galan, and L. Soriano, Appl. Surf. Sci. **526**, 146699 (2020).
[21] V. Nistor, L. A. Gonzalez, L. Aguilera, I. Montero, L. Galan, U. Wochner, and D. Raboso, Appl. Surf. Sci. **315**, 445 (2014).
[22] S. Mori, M. Yoshida, and D. Satoh, Phys. Rev. Accel. Beams **24**(2), 022001 (2021).
[23] X. Yang, G. Sun, B. Song, W. Han, C. Wang, W. Li, S. Zhang, F. Song, F. Zou, and G. Zhang, High Voltage **8**(4), 717–727 (2023).
[24] P. Gonzalez, C. Alcaide, R. Cervera, M. Rodriguez, O. Monerris, J. Petit, A. Rodriguez, A. Vidal, J. Vague, J. V. Morro, P. Soto, and V. E. Boria, IEEE J. Microwaves **2**(1), 57 (2022).
[25] H. Ren and Y. Xie, Int. J. RF Microwave Comput.-Aided Eng. **32**(3), e23002 (2022).
[26] S. V. Langellotti, N. M. Jordan, Y. Y. Lau, and R. M. Gilgenbach, IEEE Trans. Plasma Sci. **48**(6), 1942 (2020).
[27] A. Iqbal, P. Y. Wong, D.-Q. Wen, S. Lin, J. Verboncoeur, and P. Zhang, Phys. Rev. E **102**(4), 043201 (2020).
[28] M. Siddiqi and R. Kishek, IEEE Trans. Electron Devices **66**(7), 3162 (2019).
[29] X. C. Bo, H. Wang, Y. Zhai, X. Wang, J. F. Zhang, and T. J. Cui, IEEE Trans. Electron Devices **70**(4), 1962 (2023).
[30] N. K. Vdovicheva, A. G. Sazontov, and V. E. Semenov, Radiophys. Quantum Electron. **47**(8), 580 (2004).
[31] S. Anza, M. Mattes, C. Vicente, J. Gil, D. Raboso, V. E. Boria, and B. Gimeno, Phys. Plasmas **18**(3), 032105 (2011).
[32] A. G. Sazontov and N. K. Vdovicheva, Appl. Phys. Lett. **101**(11), 113506 (2012).
[33] F. Shen, X. Wang, W. Cui, and L. Ran, IEEE Trans. Plasma Sci. **48**(2), 433 (2020).
[34] A. G. Sazontov, V. A. Sazontov, and N. K. Vdovicheva, Contrib. Plasma Phys. **48**(4), 331 (2008).
[35] S. Anza, C. Vicente, J. Gil, V. E. Boria, B. Gimeno, and D. Raboso, Phys. Plasmas **17**(6), 062110 (2010).
[36] I. Bojko, N. Hilleret, and C. Scheuerlein, J. Vac. Sci. Technol. A **18**(3), 972 (2000).
[37] M. A. Furman and M. T. F. Pivi, Phys. Rev. Spec. Top.-Accel. Beams **5**(12), 124404 (2002).
[38] V. E. Semenov, R. Udiljak, D. Anderson, M. Lisak, and J. Puech, Phys. Plasmas **15**, 033501 (2008).


03 October 2023 13:18:37



Published under an exclusive license by AIP Publishing